

Chapter 2

Dynamical Simulation of Electron Backscatter Diffraction Patterns

Aimo Winkelmann

2.1 Introduction

To extract the maximum amount of information from experimental electron backscatter diffraction (EBSD) patterns, it is necessary to realistically model the physical processes that lead to the formation of the characteristic diffraction features in the form of Kikuchi bands and lines. Whereas the purely geometrical relations in the observed networks of bands and lines can be explained by mapping out Bragg's law for the relevant reflecting lattice planes, the dynamical theory of electron diffraction is needed to explain the observed *intensities*. This theory takes into account the fact that electrons interact strongly with matter, which leads to multiple elastic and inelastic scattering of the electron waves in a crystal.

To simulate a realistic EBSD pattern, we will need to model the very general situation of an incident electron beam which hits a sample and which subsequently undergoes elastic and inelastic interactions to result in the intensity pattern on the observation screen. The incident primary beam contains electron waves within a relatively narrow range of energies and directions (defined by the properties of the electron gun), whereas the backscattered electrons have a broad spectrum of energies (due to inelastic scattering) and are distributed over all possible directions (due to momentum changes by inelastic as well as elastic scattering). Because the exact solution of the combined elastic and inelastic

scattering problem is one of the most difficult problems in electron diffraction theory, we will use a simplified model, which is expected to capture the most important aspects of the problem.

2.2 Model of Electron Backscatter Diffraction

For a general description of the intertwined elastic and inelastic redistribution of electrons from the states of the incident beam to the outgoing states, the quantum mechanical density matrix formalism can be used (Dudarev et al. 1993). It enables one to describe in a consistent way the coherent elastic scattering that is at the heart of the diffraction process, together with the loss of energy and the increasing randomization of quantum mechanical phase relationships between the involved states by inelastic scattering. If the relevant states and scattering processes are identified, it is in principle possible to calculate the evolution of the population in those states observed on the phosphor screen in an EBSD experiment.

The density matrix formalism allows the most general description, but a full ab initio treatment of EBSD intensities is very complicated. To make the dynamical simulations useable in practical situations, we will apply a simplified model, which captures the most important aspects of the problem using some reasonable approximations. Our main approximation will be that the inelastic scattering, which produces the sources for the subsequently diffracted electrons, can be handled independently of the diffraction process in the outgoing path (Fig. 2.1). This means that no

A. Winkelmann (✉)
Max-Planck-Institut für Mikrostrukturphysik, Halle (Saale),
Germany
e-mail: winkelm@mpi-halle.mpg.de

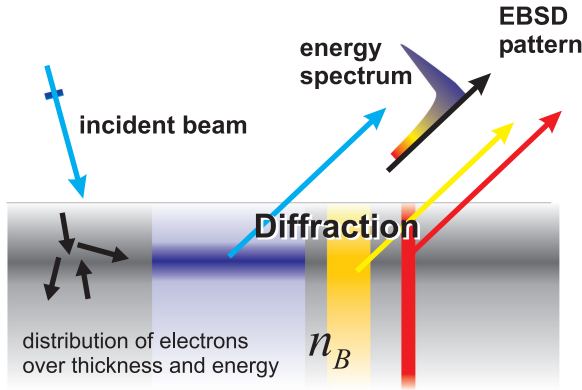


Fig. 2.1 Schematic model for the simulation of EBSD patterns: The multiple elastic and inelastic scattering of primary electrons leads to an incoherent distribution n_B of electrons over energy and thickness. The diffraction is assumed to take place independently for each energy and from each backscattering depth according to the weight function n_B

coherence between the incident electrons and the electrons forming the EBSD pattern is left. We will assume that we know the distribution $n_B(\theta, \phi, \theta_{in}, \phi_{in}, E, t)$ of inelastically scattered electrons at energy E , in a depth t inside the sample that are scattered into the direction (θ, ϕ) if the primary beam is incident from the direction (θ_{in}, ϕ_{in}) . In this way, n_B is assumed to represent the accumulated effects of elastic and inelastic scattering from the incident beam; but it also needs to include those electrons which are lost from the diffracted wave field by inelastic scattering in the outgoing path. A practical way to approximately determine $n_B(E, t)$, for instance, is by Monte Carlo simulations. We will see in the following that the observed EBSD intensity distributions can be explained without very detailed assumptions about the function n_B , because in an EBSD experiment, we are actually less interested in the absolute intensities which are inelastically scattered, but rather in the small-scale variations that are introduced by dynamical diffraction on a relatively smooth background of inelastically scattered electrons. In the following, we will assume that $n_B(E, t)$ is given and we will illustrate what consequences different depth distributions will have on the dynamical diffraction intensities.

Under the assumptions of our model, we can symbolically write down the observed intensity I_B as an integral over all inelastically scattered electrons which are diffracted in the outgoing pathway with initial

distribution function n_B from the primary energy E_p down to zero kinetic energy, and which come from the sample surface up to a maximum thickness t_{max} :

$$I_B \propto \int_0^{E_p} dE \int_0^{t_{max}} dt D[n_B(\theta, \phi, \theta_{in}, \phi_{in}, E, t)] . \quad (2.1)$$

The diffraction process of the electrons at energy E is symbolized by an operator D .

2.3 Dynamical Electron Diffraction in EBSD

According to our model, we describe the observed EBSD patterns as a superposition of diffraction patterns from electrons having a fixed energy E . The contributions from different energies are added according to the weight function n_B . In the following, we will introduce the theoretical framework necessary to describe the dynamical diffraction process.

2.3.1 Using the Reciprocity Principle

The reciprocity principle (Fig. 2.2) is based on time reversal symmetry and states that it makes no difference whether we calculate the intensity at point **D** which is due to the elastic scattering of waves emitted from point **P**, or whether we calculate the intensity at point **P** which is due to the scattering of waves emitted from point **D** (Pogany and Turner 1968).

The tremendous advantage of using the time-reversed path in Fig. 2.2b comes from the fact that in Fig. 2.2a we are detecting the intensity at a distance that is basically infinite compared to the separations of the scattering atoms. In this limit, a plane wave is detected at **D**. Turning this around, it means that we can start a *single* plane wave along the direction defined by the point **D** and then we calculate how this single plane wave is scattered by the atoms of the sample. For perfect crystals, the Bloch wave theory is a convenient method to solve this problem. It turns out that by this approach we not only obtain the wave function at a single point **P**, but instead, in a single run we get the wave function in the whole crystal. In this way, we

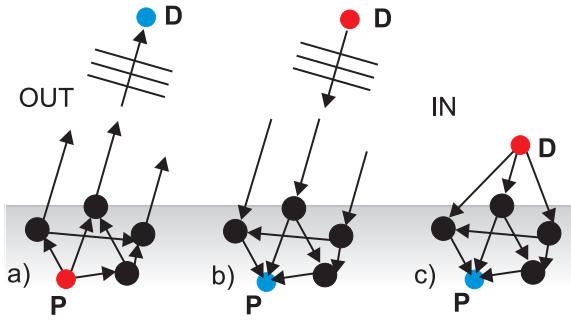


Fig. 2.2 Application of the reciprocity principle for EBSD calculations: (a) EBSD patterns are formed by elastic scattering of electrons which are emitted into *all* directions from a point source at **P**. These electrons are detected at point **D** on the phosphor screen, which is practically infinitely far away. In this limit, a plane wave is detected. (b) The problem (a) is equivalent to starting a plane wave in a *single* direction from **D** and detecting the intensity arriving at point **P**. (c) The big advantage of calculating the time-reversed problem in (b) stems from the fact that we need only one initial plane wave. This advantage would be lost if **D** is near the crystal surface and we would have to consider waves emitted into all directions whether we start the calculation from **D** or from **P**

are able to analytically integrate the effects of different emitters from various depths and positions in the unit cell.

The reciprocity principle can be used to connect the dominant outgoing diffraction process in EBSD to other types of methods that are governed by the diffraction of ingoing electrons. This includes electron-channelling patterns, where the total number of backscattered electrons is monitored as a function of the incidence angle of an electron beam. Important conclusions for EBSD can be drawn from previous studies of electron channelling patterns by the dynamical theory (Marthinsen and Høier 1986, 1988; Rossouw et al. 1994; Dudarev et al. 1995). Another close connection can be seen between EBSD and methods of transmission electron microscopy (TEM). To describe TEM, the diffraction and corresponding modulation in intensity of transmitted plane waves needs to be calculated. Obviously, this is related to the problem illustrated in Fig. 2.2b, with the principal difference that in TEM, the relevant thickness is the thickness of the sample; whereas in EBSD, the plane wave needs to be evaluated at the thickness of the emitter at point **P**.

There exists a number of computational approaches to describe the diffraction of transmitted electrons. These approaches include most prominently the mul-

tislice and the Bloch wave approaches. One can in principle use these existing approaches for TEM simulations to also simulate EBSD patterns (disregarding numerical limitations). We just have to appropriately account for the property of the diffracted wave field that is observed in EBSD: the *probability density inside the crystal* at the atomic positions **P**.

2.3.2 Bloch Wave Formalism

In our simulations, we will apply the Bloch wave approach. This theory solves the diffraction problem for electrons in a perfect crystal lattice by exploiting the fact that the wave function must have a very specific form in a three-dimensionally periodic potential. The use of this method is described in several accessible reviews (Humphreys 1979; Spence and Zuo 1992). In the following we will summarize the most important aspects.

The wave function inside the crystal is described as a superposition of Bloch waves with wave vectors $\mathbf{k}^{(j)}$

$$\Psi(\mathbf{r}) = \sum_j c_j \exp(2\pi i \mathbf{k}^{(j)} \cdot \mathbf{r}) \sum_g C_g^{(j)} \exp(2\pi i \mathbf{g} \cdot \mathbf{r}). \quad (2.2)$$

The aim of this approach is to get the expansion coefficients c_j and $C_g^{(j)}$, as well as the $\mathbf{k}^{(j)}$. After this is accomplished, the wave function Ψ is known and, in the next step, the coupling of the inelastic scattering processes to the diffractionally modulated probability amplitude Ψ is taken into account.

The wave function Ψ is a solution of the Schrödinger equation for an incident plane wave $\exp(2\pi i \mathbf{K}_0 \cdot \mathbf{r})$, corresponding to an energy of $\hbar^2 K_0^2 / 2m$:

$$\frac{-\hbar^2}{8\pi^2 m} \Delta \Psi(\mathbf{r}) - |e| V(\mathbf{r}) \Psi(\mathbf{r}) = \frac{\hbar^2 K_0^2}{2m} \Psi(\mathbf{r}). \quad (2.3)$$

To proceed with the determination of Ψ , one uses the translational invariance of the crystal to write the potential as a Fourier series:

$$U(\mathbf{r}) = U^c(\mathbf{r}) + iU'(\mathbf{r}) = \sum_{\mathbf{g}} U_{\mathbf{g}} \exp(i2\pi \mathbf{g} \cdot \mathbf{r}). \quad (2.4)$$

U is a scaled potential which is measured in \AA^{-2} and which is formed from complex electron structure factors $U_{\mathbf{g}}^c = 2m|e|V_{\mathbf{g}}/h^2$, with $V_{\mathbf{g}}$ being a Fourier coefficient of the crystal potential in volts and the relativistic electron mass m . The loss of electrons from the diffracted coherent population due to inelastic effects is taken into account by corresponding Fourier coefficients $U_{\mathbf{g}}'$ of an imaginary part of the crystal potential.

Substitution of these expressions for the wave function and the potential into the Schrödinger equation leads to the standard dispersion relation:

$$[\mathbf{K}^2 - (\mathbf{k}^{(j)} + \mathbf{g})^2]C_{\mathbf{g}}^{(j)} + \sum_{\mathbf{h}} U_{\mathbf{g}-\mathbf{h}}C_{\mathbf{h}}^{(j)} = 0. \quad (2.5)$$

\mathbf{K} is the incident electron wave vector inside the crystal, $K_0^2 = K^2 - U_0^c$, with the mean inner potential U_0^c and the electron wave vector in vacuum \mathbf{K}_0 .

Then $\mathbf{k}^{(j)}$ is written as:

$$\mathbf{k}^{(j)} = \mathbf{K} + \lambda^{(j)}\mathbf{n}, \quad (2.6)$$

where \mathbf{n} is a unit vector normal to the surface. One can then transform (2.5) into an eigenvalue problem, which gives the eigenvalues $\lambda^{(j)}$ and eigenvectors with elements $C_{\mathbf{g}}^{(j)}$ (Spence and Zuo 1992). This includes the effects due to the tilt of the outgoing direction with respect to the surface (Allen and Rossouw 1989) and is also valid for reciprocal space vectors \mathbf{g} in higher order Laue zones (HOLZ). The boundary conditions at the surface determine the coefficients c_j in (2.2). These quantities are given by the elements of the first column of the inverse of the matrix whose elements are $C_{\mathbf{g}}^{(j)}$. After this, the wave function (2.2) is known.

The Fourier coefficients of the real and the imaginary part of the crystal potential can be calculated from the contributions of the atoms that constitute the unit cell. These contributions can be obtained from published parameterizations for the real and imaginary part of the potential (Weickenmeier and Kohl 1991).

The eigenvalue method described above scales as N^3 with the number N of the included reflecting planes. This quickly leads to impractically long computation times if a large number of reflections has to be included. This can be overcome by the use of the Bethe perturbation scheme, which allows the inclusion of the effects of weak reflections U_h by the transformation into an effective potential of the strong beams $U_{\mathbf{g}}^{\text{eff}}$

without increasing the matrix dimensions:

$$U_{\mathbf{g}}^{\text{eff}} = U_{\mathbf{g}} - \sum_{\mathbf{h}} \frac{U_{\mathbf{h}}U_{\mathbf{g}-\mathbf{h}}}{2K S_h}, \quad (2.7)$$

where $2K S_h$ is defined by $2K S_h = K^2 - (\mathbf{K} + \mathbf{h})^2$, containing the excitation error S_h . For the use of the Bethe perturbation, beam selection and convergence criteria have been developed in the context of convergent beam electron diffraction (Zuo and Weickenmeier 1995). Strong and weak beams are selected according to their structure factor and the excitation error, describing how strong the influence of a certain reflecting plane is at the considered point in the diffraction pattern.

2.3.3 Inclusion of the Backscattering Process

Using the Bloch wave approach, we can determine the diffraction-induced changes in the probability of an electron to leave the crystal from an arbitrary position \mathbf{r} inside the crystal. The backscattered electrons start predominantly from the positions of the atoms. In a first approximation, this simply means that we need to calculate the probability density $\Psi\Psi^*$ at the atomic positions \mathbf{P} . This is straightforward by using Equation (2.2) (Allen and Rossouw 1989). For arbitrary inelastic processes, the interaction of diffracted electrons with the crystal can be modelled by generalized potentials (Allen and Rossouw 1990). In the case of backscattering, these potentials have the form of delta functions (point sources), which are broadened by the thermal vibrations. The dynamically backscattered intensity integrated from depth t_1 to t_2 is then given by (Rossouw et al. 1994):

$$I_{\text{DYN}} \propto \sum_{n,ij} Z_n^2 B^{ij}(t_1, t_2) \sum_{\mathbf{g},\mathbf{h}} C_{\mathbf{g}}^{(i)} C_{\mathbf{h}}^{(j)*} \times \exp(-B_n s^2) \exp[2\pi i(\mathbf{g} - \mathbf{h}) \cdot \mathbf{r}_n], \quad (2.8)$$

with atoms at \mathbf{r}_n , Debye-Waller factors $\exp(-B_n s^2)$, and a depth integrated interference term $B^{ij}(t_1, t_2)$ of

the Bloch waves i and j :

$$B^{ij}(t_1, t_2) = c_i c_j^* \frac{\exp[2\pi i(\lambda^i - \lambda^{j*})t_2] - \exp[2\pi i(\lambda^i - \lambda^{j*})t_1]}{2\pi i(\lambda^i - \lambda^{j*})}. \quad (2.9)$$

Because the wave functions are known to be of the form in Equation (2.2), the thickness integration for an inelastic source extending from t_1 to t_2 can be carried out analytically.

Using the method described above, the backscattering pattern can be calculated point by point, each describing a well-defined wave vector direction \mathbf{K}_0 . The application of the Bethe perturbation scheme allows the inclusion of a large number of reflecting planes, so that the large viewing angles in EBSD can be handled (Winkelmann et al. 2007).

2.4 Applications

In this section we will apply the developed computational approach to a number of important basic problems of the EBSD technique.

2.4.1 A Real-Space View of EBSD

To illustrate the basic mechanism behind a typical intensity distribution in Kikuchi bands, we calculated a hypothetical nine-beam EBSD pattern of the $\{110\}$ and $\{200\}$ families of lattice planes from bcc iron, which is shown in the top middle part of Fig. 2.3. It is one of the very useful properties of the Bloch wave approach that we can selectively switch off all other lines in the diffraction pattern because of the one-to-one correspondence between the Fourier coefficients (reciprocal lattice vectors) considered in the many-beam problem and the observed Kikuchi lines. For the simplified EBSD pattern shown in Fig. 2.3, we can now calculate the probability density in the crystal that corresponds to some typical points in the Kikuchi bands. Because the considered lattice planes are perpendicular to the surface, we can show the probability density averaged along the $[001]$ surface normal direction as a two-dimensional plot over 3×3 unit cells in the other

panels of Fig. 2.3. The crystal surface is viewed from the direction of the surface normal, the centered atoms of the bcc cells are drawn smaller.

In the right part of Fig. 2.3, we see the probability density corresponding to the middle (d, blue dashed) and to the border (c, red dashed) of a $\{200\}$ Kikuchi band. It is clearly seen that in the middle of the Kikuchi band, the probability density is concentrated at the atomic positions; while at the border of the band, the probability density is focused between the atomic planes. The same process happens for the $\{110\}$ Kikuchi band in the left part of Fig. 2.3, a and b. One sees how nicely the diffracted probability density has to conform to the symmetry implied by the respective lattice planes. This becomes particularly important near the zone axis in the center (e) of the EBSD pattern, where the full interaction of all crossing lattice planes has to be considered. Correspondingly, the probability density is confined to the channel along the $[001]$ atomic columns (lower middle panel of Fig. 2.3; the remaining intensity between the atoms is due to the limited number of 9 beams in the calculation).

From the probability density of diffraction we can draw conclusions regarding the observed intensity in a typical EBSD pattern. There will be high intensity in the pattern in directions where the diffraction probability density overlaps strongly with those places where the inelastic electrons are created. These places coincide with the atomic positions in the case of thermal diffuse (phonon) scattering. In summary, this means that we should see high intensity in the middle of the Kikuchi bands (probability density is focused mainly on the atomic planes), and low intensity at the border (probability density is mainly between the atomic planes).

This explanation suffices for the majority of EBSD patterns taken in standard setups with incidence angles in the order of 70 degrees. However, under special experimental circumstances, a contrast reversal of the observed Kikuchi bands can take place, and the above explanation has to be extended. In early investigations of Kikuchi patterns, it has been observed that the contrast within a band is reversed for electrons leaving the sample with low take-off angles when the *incidence* angle of the electron beam is decreased so that it impinges more steeply on the surface (Alam et al. 1954). In such a situation, the backscattered electrons come from a larger depth below the sample surface (Reimer 1998). Similar contrast reversals of Kikuchi

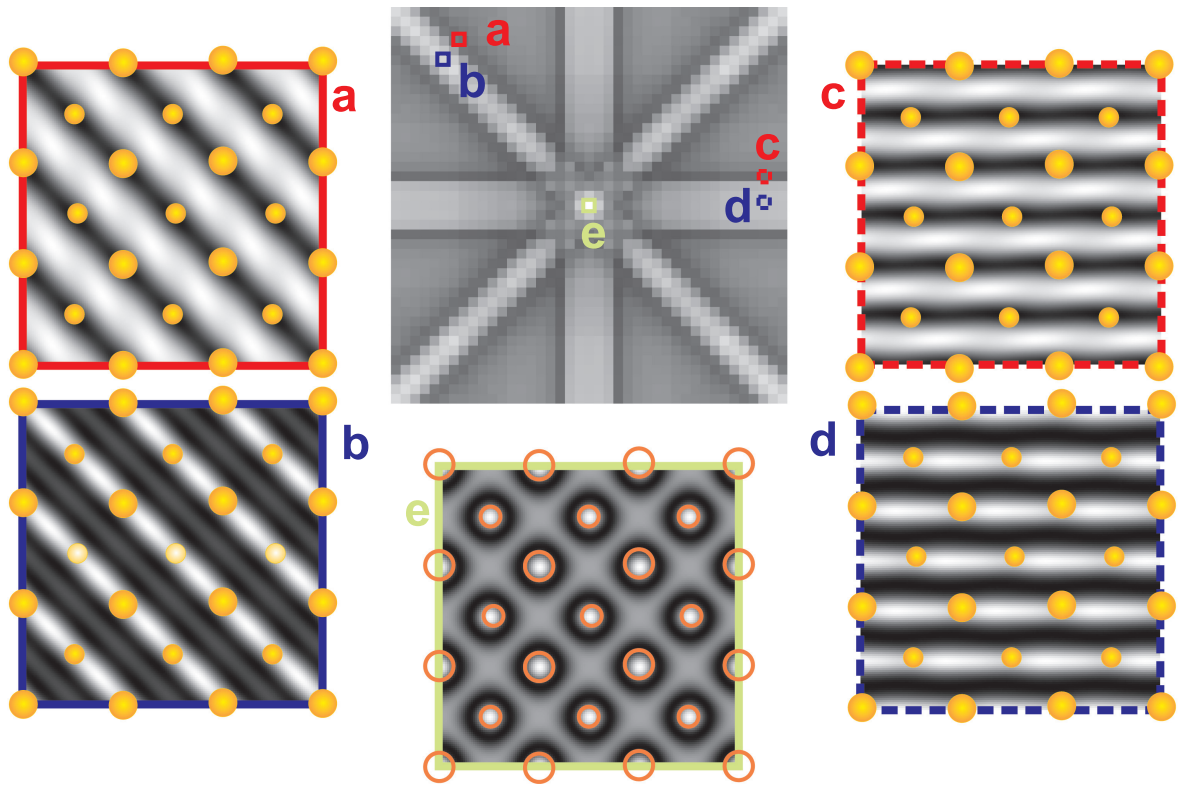


Fig. 2.3 Nine-beam EBSD pattern (*top middle*) of a bcc structure and diffraction probability distributions at selected directions, which are marked by *solid and dashed colored squares* in

the diffraction pattern. The centered atoms in the bcc structure are drawn smaller

bands have also been observed in transmission electron microscopy, and theoretical models for the thickness dependent contrast reversal of Kikuchi bands in transmission electron diffraction were given (Hall 1970; Chukhovskii et al. 1973).

In the dynamical theory, the contrast reversal with thickness appears due to the much stronger absorption of those Bloch waves which travel along the atomic positions, compared to the Bloch waves which travel between the atomic planes. This has an important consequence if we increase the depth from which the electron waves start the backscatter diffraction process.

This is illustrated in Fig. 2.4 by a simple model calculation, similar to the real-space view of Fig. 2.3. This calculation was carried out for a source which is near the surface (upper part) and another source which is deeper inside the crystal (lower part). In the middle

we see the calculated Kikuchi band intensity. On the left of Fig. 2.4, we see the type II wave field which is excited predominantly at the edges of a Kikuchi band. On the right side of Fig. 2.4, we see the type I wave excited in the middle part of a Kikuchi band. We emphasize that the elastic diffraction effect of the excitation of two different types of Bloch waves is *not* a function of thickness. What changes is the number of electrons in both types of fields: in the upper part, both fields are excited almost equally, and the increased overlap of the type I field on the right with the backscattering atoms leads to a high intensity in the middle of the band. In the situation in the lower part of the figure, although the type I wave field geometrically still overlaps better with the atomic positions, this wave field is of very low intensity because it is absorbed strongly. Effectively, the smaller residual overlap of the type II field with the backscattering

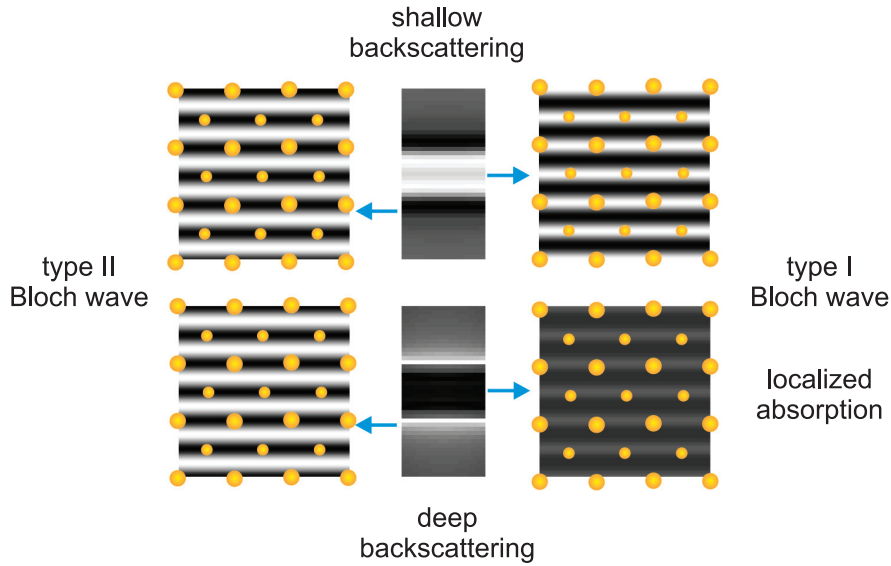


Fig. 2.4 Principle of contrast reversal with increasing thickness. The type I Bloch wave is localized at the atomic planes and is also more strongly absorbed. Beyond a certain thickness,

the type I wave is almost completely absorbed. Because the type I wave dominates in the middle of the band, there will be a minimum of intensity for a deep source

atoms on the right still leads to a higher signal on the edges of the Kikuchi band from the deeper source. Correspondingly, we observe a Kikuchi band with inverted contrast.

2.4.2 Full Scale Simulation of EBSD Patterns

We now demonstrate that by inclusion of all relevant lattice planes in a dynamical calculation, we can simulate a complete EBSD pattern with very good agreement to experimentally measured patterns.

As a first example, we choose molybdenum, with a bcc structure and a lattice constant of 3.147 \AA . The Debye-Waller factor B was assumed to be 0.25 \AA^2 (Peng et al. 1996), and all reflections which appear within 50 degrees from the $[001]$ zone axis to have a minimum lattice spacing of $d_{hkl} > 0.35 \text{ \AA}$ and a minimum structure amplitude $U_{hkl} > 0.005 \text{ \AA}^{-2}$. This leads to a set of about 1200 beams, which need to be taken into account. On average, about 150 beams were treated exactly in the many-beam problem, the rest were taken into account by the Bethe perturbation. We assumed that backscattered electrons were excited from a thickness up to 150 nm. The final

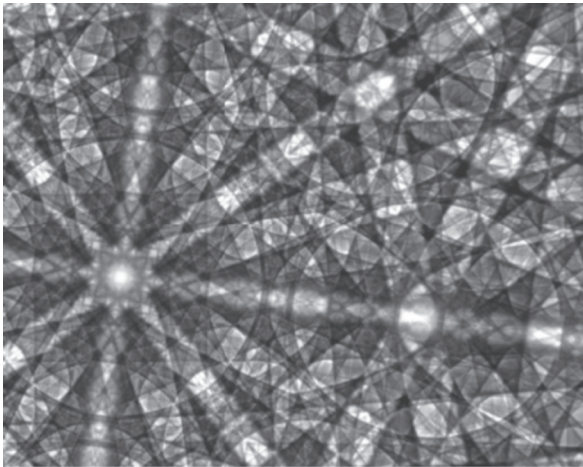
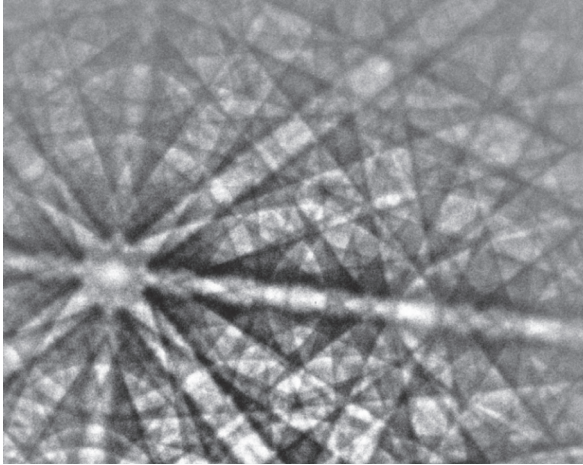
simulated picture has been smoothed according to an angular resolution of about 1 mrad. The contrast has been changed very slightly to correspond to the measured pattern. The calculation was carried out for 640×480 data points and took 3.5 days on a single CPU of a Pentium D 3.4 GHz processor.

In Fig. 2.5, we show the comparison with an experimental pattern taken at 25 keV incident beam energy. Apart from the increased noise in the outer parts of the experimental pattern, it can be seen that the simulation and the experiment match almost perfectly. Also, the typical ring structures appear in the dynamical calculation. The mechanism that leads to the formation of the rings can be interpreted as a transmission resonance and has been extensively discussed for the case of an incident plane wave, which at the resonance angle θ_r strongly couples to states bound in the atomic column along the respective zone axis (Dudarev and Peng 1993b, a). By reciprocity, we can see that this effect works analogously for the coupling between Bloch waves moving in the potential of an atomic column and outgoing plane waves, which form the ring intensity near the angle θ_r .

The specific reciprocal lattice vectors that label the Fourier coefficients of the crystal potential involved in the transfer of intensity between the atomic column

Mo 25kV

experiment



simulation

Fig. 2.5 Full scale many-beam dynamical simulation of an EBSD pattern from molybdenum and comparison with an experimental pattern. In the calculation, a total of 1200 reflections were considered; on average 150 reflections were treated exactly, the others were included by perturbation. A lattice constant of $c = 3.147 \text{ \AA}$ was used (experimental pattern courtesy of E. Langer)

and the ring have non-zero components along the respective zone axis. This is why the rings in EBSD patterns have been termed “HOLZ rings” for short (Higher Order Laue Zone). Measuring the diameter of the HOLZ rings allows the estimation of lattice constants, which has been shown to be useful for phase identification using EBSD patterns (Michael and Eades 2000). Due to the inherently many-beam nature of the HOLZ ring effect, it is expected that corresponding dynamical simulations can be additionally applied to

extract high precision lattice parameters from measured rings.

2.4.3 The Influence of the Energy Spectrum of the Backscattered Electrons

In view of the good agreement of the simulation shown in Fig. 2.5 with the experiment, it is necessary to analyze the influence of the energy spectrum of the backscattered electrons on the diffraction pattern. We saw that the simulation done at the energy level of the incident electrons with inclusion of a limited angular resolution does in fact match quite nicely to the experiment. Obviously, electrons in a relatively limited energy range below the incident beam energy are decisive for most of the observed diffraction features. Since the width of a Kikuchi band is a function of the energy of the diffracted electrons, an increasingly broader energy spectrum will tend to wash out the diffraction features. A limit on the energy spread which is compatible with an EBSD pattern can be estimated by comparison of the finest structures in the experimental pattern with dynamical simulations that are integrated for a range of energies. We will investigate such a scenario for the case of GaN thin films, which show very detailed patterns.

The simulations have been carried out for a limited field of view of about 25 degrees centered around the $[0\bar{2}1]$ zone axis. We took into account 431 reflectors with a lattice spacing of $d_{hkl} > 0.3 \text{ \AA}$ and a structure amplitude $U_{hkl} > 0.005 \text{ \AA}^{-2}$. The Debye-Waller factor B was assumed at 0.25 \AA^2 . The calculations were done for 300×300 pixels in 50 eV steps, starting from the incident beam energy of 20 kV down to 15 kV.

The experimental pattern is shown in Fig. 2.6e. We see simulated patterns for the energies of 20 kV, 19.5 kV, and 18.5 kV in parts a, b, and c, respectively. By comparing these simulations with the experiment, one immediately recognizes that the central dark spot in the center of the $[0\bar{2}1]$ zone axis is becoming smaller with energy, and at 18.5 kV is already smaller than observed in experiment. A further reduction of the relevant energy range is supported by the feature which is indicated by the arrows. This feature is located near the HOLZ ring around the $[0\bar{2}1]$ zone axis, and it is

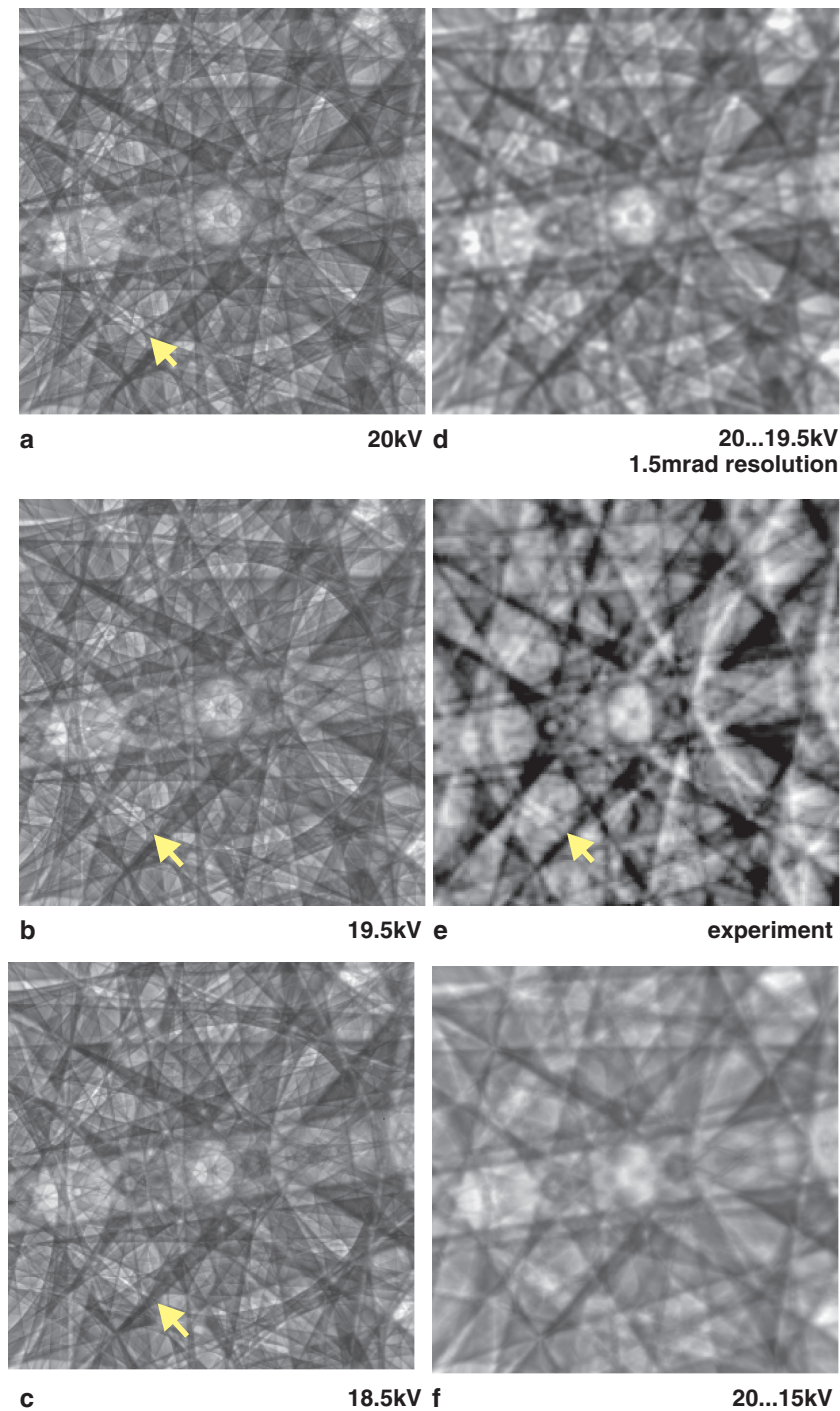


Fig. 2.6 Estimation of the influence of an energy spread in EBSD from GaN: (a, b, c) calculations at the specified energies (without any image processing). Note the delicately changing fine structure in the zone axis in the center of the ring, as well as the change in the feature at which the arrows are pointing. (d)

average of 11 diffraction patterns in 50 eV steps, from 20 kV to 19.5 kV, with angular averaging according to 1.5 mrad resolution. (e) experimental pattern from GaN with incident beam voltage of 20 kV (courtesy of A. P. Day). (f) average of 100 diffraction patterns from 20 kV to 15 kV

very sensitive to the electron energy. In the experiment, we notice a gap in the intensity distribution of this feature. In the simulation, we see this gap opening at about 19.5 kV, whereas it is clearly closed at 18.5 kV. In this way, observation of the fine structure in the pattern has given us a clear indication that electrons in the range of 20 kV to 19.5 kV dominate in producing the observed features. In order to see how the averaging of such an energy spread compares to the experiment, we summed 11 patterns in 50 eV steps from 20 kV to 19.5 kV, and we applied an additional angular averaging according to a 1.5 mrad angular resolution. This additional angular broadening takes into account the limited pixel size of the CCD camera plus a possible additional angular smearing of the intensity due to lattice defects and surface contamination. The averaged simulated pattern compares very well with the experimental observations. Taking into account that we have not used any information about the experimental energy spectrum (we assumed $n_B = 1$ for 19.5 . . . 20 kV), the possibility of obtaining good agreement with the experiment in a calculation for a single or a very limited number of energies would greatly reduce the required computation times. Our observation compares nicely to experimental observations using energy-filtered EBSD from Si samples. It was found that low loss electrons with energies not less than about 3% of the primary beam are predominant in producing the observed contrast (Deal et al. 2008).

We have seen that the comparison of experimental and simulated energy dependent fine structure in EBSD patterns allows important conclusions regarding the energy spectrum. In many cases, however, EBSD patterns do not show such relatively sharp features as in Fig. 2.6e. This is not necessarily due to a broad energy spectrum, but can also be caused, e.g., by lattice imperfections. From very general considerations, we can expect higher density materials to show a broader energy spectrum due to the increased multiple inelastic scattering (Reimer 1998). This then should correlate with a reduced fine structure in these materials. As an extreme case, we illustrate in Fig. 2.6f that even an energy spread of 5 kV, from 15 kV to 20 kV (100 patterns in 50 eV steps), still leads to pronounced Kikuchi bands with an overall character that might resemble experimental patterns from some materials with not as much fine structure as GaN or Si. It seems that a rather broad energy spectrum is compatible with EBSD patterns that do not show higher order fine structure. In

turn this would mean that energy filtering would produce significantly more detail if the loss of fine structure were caused by energy broadening alone (whereas energy filtering would not help if the fine structure is lost due to lattice imperfections). More systematic insight is expected in the future if realistic Monte Carlo simulations of inelastic scattering are coupled with the many-beam dynamical simulations.

2.4.4 Dynamical Effects of Anisotropic Backscattering

In this section we will show which qualitative changes appear in the EBSD patterns if we take into account that the incident electrons are backscattered with different intensity in different directions. The scattering at high kinetic energies is strongly enhanced in the forward direction. Due to the usual geometry of EBSD experiments using relatively shallow incidence angles, a significant anisotropy of the initial distribution of the inelastically scattered electrons with respect to the detected directions is created. This directly influences the overall intensity distribution of the observed EBSD pattern neglecting any diffraction effects: the patterns show higher intensity towards the forward scattering direction and significantly decrease in intensity towards larger backscattering angles. However, within the small angular range of the Kikuchi band cross sections that we are interested in, this will be a relatively smoothly varying background, which can be removed by flat-fielding techniques used for enhancing the diffraction contrast in experimental patterns.

The anisotropy of each distinctive backscattering event (emitting an anisotropic coherent wave) also enters into the dynamical diffraction problem. This results in selective enhancement or suppression of the intensity of Kikuchi lines as a function of their orientation with respect to the incoming beam direction. The mechanism of these excess and deficiency lines has been discussed for the case of transmission electron microscopy Kikuchi patterns (Kainuma 1955).

The excess lines usually appear at scattering angles, which are farther away from the incident beam direction than the deficiency lines. If the backscattered electrons with wave vectors near the incident beam direction have a higher intensity than the wave vectors

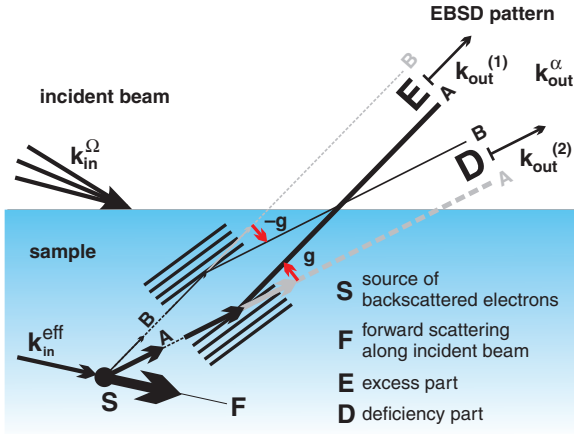


Fig. 2.7 Mechanism of the formation of excess and deficiency lines in EBSD patterns

for larger scattering angles, the intensity is then asymmetrically removed by diffraction from the position of the deficiency line and transferred to the excess line.

In Fig. 2.7, we show the basic ingredients that are necessary to qualitatively understand the excess-deficiency effect in electron backscatter diffraction.

The sources **S** of backscattered electrons are localized at atomic positions inside the crystal. The creation of the backscattered electron waves is not isotropic, and a single electron is scattered into the directions **A** and **B** with different probabilities. What is important for the effect is only that a difference exists between the numbers of electrons that are initially excited into the different directions **A** and **B**. Subsequently, these electrons are dynamically diffracted by the surrounding crystal lattice. In Fig. 2.7, we show the case that beams along **A** will be scattered by lattice plane **g**, whereas beams along **B** will be scattered by **-g**, corresponding to a pair of Kikuchi lines, with a band of increased intensity between them. The intensities along $\mathbf{k}_{out}^{(1)}$ and $\mathbf{k}_{out}^{(2)}$ in the EBSD pattern can be thought to be formed by electrons that are moving into these directions without scattering, plus electrons that are dynamically scattered from other initial directions into these final directions. Assuming equally strong scattering by **g** and **-g**, the dynamical diffraction problem is perfectly symmetric. Correspondingly, the dynamically diffracted intensities in the directions $\mathbf{k}_{out}^{(1)}$ and $\mathbf{k}_{out}^{(2)}$ would not show an excess-deficiency asymmetry if we had the same number of **A** and **B** electrons. Now we consider the case in which **A** is initially stronger

than **B**. When there are more **A** electrons than there are **B** electrons, a higher number of electrons is necessarily scattered by **g** away from the initial direction of the **A** electrons into the direction $\mathbf{k}_{out}^{(1)}$, than the number of **B** electrons scattered by **-g** from $\mathbf{k}_{out}^{(1)}$ back to the initial **A** direction $\mathbf{k}_{out}^{(2)}$. By this mechanism more intensity ends up in direction $\mathbf{k}_{out}^{(1)}$ than in direction $\mathbf{k}_{out}^{(2)}$, and the excess **E** and deficiency **D** features are formed.

We have demonstrated a simple and transparent way to incorporate the relevant effects of anisotropic backscattering into Equation (2.8) (Winkelmann 2008). It was assumed that the beams **g** are excited with different strengths according to a function χ that depends on **g** and the incident and detected beam directions:

$$f_n(\mathbf{q} + \mathbf{g}) \propto Z_n \cdot \chi_g(\mathbf{k}_{in}, \mathbf{k}_{out}^\alpha). \quad (2.10)$$

For simplicity, we assumed that the relative strength of excitation shows a Gaussian distribution as a function of wave-vector transfer **q** from some effective incident beam direction \mathbf{k}_{in}^{eff} :

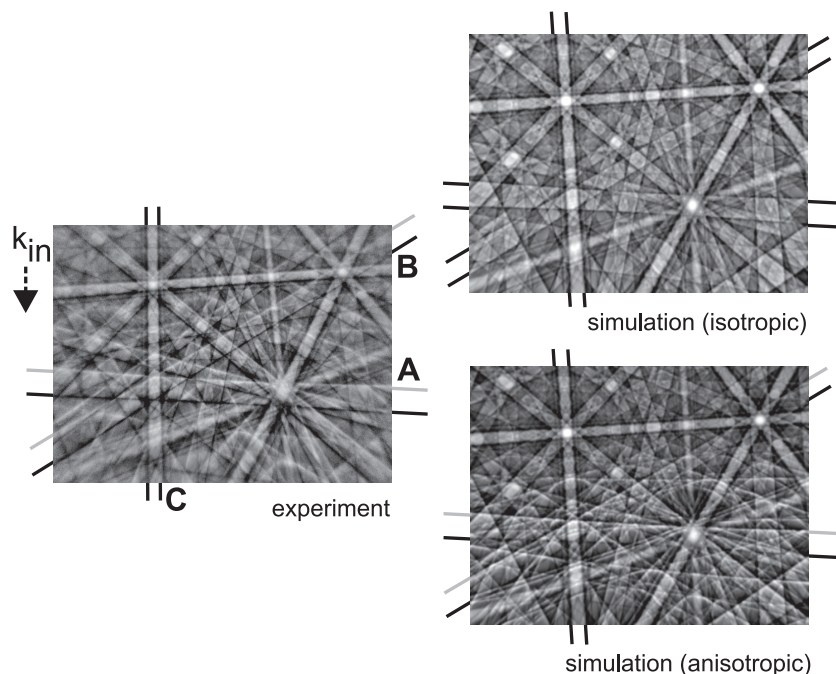
$$\chi_g = 1 + a \cdot \exp\left(\frac{-(\mathbf{k}_{out}^\alpha - \mathbf{k}_{in}^{eff} + \mathbf{g})^2}{b^2}\right). \quad (2.11)$$

In this equation, $\mathbf{q} = \mathbf{k}_{out}^\alpha - \mathbf{k}_{in}^{eff}$. The phenomenological parameters *a*, *b*, and \mathbf{k}_{in}^{eff} have to be chosen for best agreement with the experiment. The factor χ_g describes the deviation from isotropic scattering, which is obtained by setting all $\chi_g = 1$. With this, a refined version of Equation (2.8) results:

$$I_{DYN}^{ED}(\mathbf{k}_{in}^{eff}, \mathbf{k}_{out}^{eff}) \propto A \sum_{n,ij} Z_n^2 B^{ij}(t) \times \sum_{\mathbf{g},\mathbf{h}} \chi_g \chi_h C_{\mathbf{g}}^{(i)} C_{\mathbf{h}}^{(j)*} \exp(-B_n s^2) \exp[2\pi i(\mathbf{g}-\mathbf{h}) \cdot \mathbf{r}_n] \quad (2.12)$$

This very simplified model shows the basic properties necessary for the appearance of excess-deficiency features in a transparent way, without increasing the computational load beyond practical limits and without relying on the exact microscopic details. A comparison of the isotropic and anisotropic models with an experimental pattern from CaF₂ is shown in Fig. 2.8. The simulation has been carried out at 19.5 kV using a lattice constant of 5.471 Å, including 673 reflections with a lattice spacing of $d_{hkl} > 0.3\text{Å}$ and a structure amplitude $U_{hkl} > 0.005\text{Å}^{-2}$. The Debye-Waller factor

Fig. 2.8 Excess-deficiency effect in EBSD from CaF_2 at 20 kV. *Left*: experimental pattern. *Right*: simulation for an isotropically emitting source (*top*) and for an anisotropic source (*bottom*). The gray and black lines indicate the relative difference between excess and deficient intensity. The excess-deficiency effect is semi-quantitatively reproduced by the anisotropic model (experimental pattern courtesy of G. Nolze)



B was assumed to be 0.4\AA^2 . We assumed an angular broadening of 1.5 mrad. For the excess-deficiency model, we used $a = 5000$ and $b = 4.9\text{\AA}^{-1}$. The anisotropic model reproduces very well the qualitative changes that are caused by the excess-deficiency effect. The effect resembles an illumination from the top, which corresponds to the incident beam direction. Our model also reproduces the observation that not all lines are affected equally by the excess-deficiency effect: line pair C in Fig. 2.8, which runs almost parallel to the incident beam direction, is not affected much because the inelastic scattering in our model is rotationally symmetric around the effective incident beam direction. This leads to nearly equal intensity scattered by the corresponding \mathbf{g} and $-\mathbf{g}$ reflections of the line pair C.

2.5 Summary

We have seen how the Bloch wave approach can be used for a dynamical many-beam description of EBSD patterns. Very good agreement between experiment and simulation is reached in a number of cases. In the future, such dynamical simulations might become

a useful tool to push the EBSD technique to new limits in the characterization of materials.

Acknowledgements I would like to thank Carol Trager-Cowan (University of Strathclyde, Glasgow) for starting my involvement with EBSD. Austin P. Day and Gert Nolze are acknowledged for supplying experimental patterns and for inspiring discussions on various aspects of electron backscatter diffraction. Part of this work was supported by the Royal Society of Edinburgh.

References

- Alam MN, Blackman M, Pashley DW (1954) High-angle Kikuchi patterns. *Proc R Soc Lond A* 221(1145):224–242, URL <http://www.jstor.org/stable/100898>
- Allen LJ, Rossouw CJ (1989) Effects of thermal diffuse scattering and surface tilt on diffraction and channeling of fast electrons in CdTe. *Phys Rev B* 39(12):8313–8321, DOI 10.1103/PhysRevB.39.8313
- Allen LJ, Rossouw CJ (1990) Absorptive potentials due to ionization and thermal diffuse scattering by fast electrons in crystals. *Phys Rev B* 42(18):11,644–11,654, DOI 10.1103/PhysRevB.42.11644
- Chukhovskii FN, Alexanjan LA, Pinsker ZG (1973) Dynamical treatment of Kikuchi patterns. *Acta Cryst A* 29:38, DOI 10.1107/S0567739473000094
- Deal A, Hooghan T, Eades A (2008) Energy-filtered electron backscatter diffraction. *Ultramicroscopy* 108:116–125, DOI 10.1016/j.ultramic.2007.03.010

- Dudarev SL, Peng LM (1993a) Effects of bulk resonance diffraction on inelastic scattering of high energy electrons by crystals. *Proc R Soc Lond A* 440:117–133, DOI 10.1098/rspa.1993.0007
- Dudarev SL, Peng LM (1993b) Theory of bulk resonance diffraction in THEED. *Proc R Soc Lond A* 440:95–115, DOI 10.1098/rspa.1993.0006
- Dudarev SL, Peng LM, Whelan MJ (1993) Correlations in space and time and dynamical diffraction of high-energy electrons by crystals. *Phys Rev B* 48:13,408, DOI 10.1103/PhysRevB.48.13408
- Dudarev SL, Rez P, Whelan MJ (1995) Theory of electron backscattering from crystals. *Phys Rev B* 51:3397, DOI 10.1103/PhysRevB.51.3397
- Hall CR (1970) On the thickness dependence of Kikuchi band contrast. *Phil Mag* 175:63–72, DOI 10.1080/14786437008228151
- Humphreys CJ (1979) The scattering of fast electrons by crystals. *Rep Prog Phys* 42(11):1825–1887, DOI 10.1088/0034-4885/42/11/002
- Kainuma Y (1955) The theory of Kikuchi patterns. *Acta Cryst* 8:247, DOI 10.1107/S0365110X55000832
- Marthinsen K, Høier R (1986) Many-beam effects and phase information in electron channeling patterns. *Acta Cryst A* 42:484–492, DOI 10.1107/S0108767386098835
- Marthinsen K, Høier R (1988) Determination of crystal symmetry from electron channeling patterns. *Acta Cryst A* 44:693–700, DOI 10.1107/S0108767388003538
- Michael JR, Eades JA (2000) Use of reciprocal lattice layer spacing in electron backscatter diffraction pattern analysis. *Ultramicroscopy* 81:67–81, DOI 10.1016/S0304-3991(99)00119-9
- Peng LM, Ren G, Dudarev SL, Whelan MJ (1996) Debye-Waller factors and absorptive scattering factors of elemental crystals. *Acta Crystallographica Section A* 52(3):456–470, DOI 10.1107/S010876739600089X
- Pogany AP, Turner PS (1968) Reciprocity in electron diffraction and microscopy. *Acta Cryst A* 24:103–109, DOI 10.1107/S0567739468000136
- Reimer L (1998) Scanning electron microscopy—physics of image formation and microanalysis. Springer Verlag, Berlin
- Rossouw CJ, Miller PR, Josefsson TW, Allen LJ (1994) Zone axis backscattered electron contrast for fast electrons. *Phil Mag A* 70(6):985–998, DOI 10.1080/01418619408242944
- Spence JCH, Zuo JM (1992) Electron microdiffraction. Plenum Press, New York
- Weickenmeier A, Kohl H (1991) Computation of absorptive factors for high energy electron diffraction. *Acta Cryst A* 47:590–597, DOI 10.1107/S0108767391004804
- Winkelmann A (2008) Dynamical effects of anisotropic inelastic scattering in electron backscatter diffraction. *Ultramicroscopy* 108:1546–1550, DOI 10.1016/j.ultramic.2008.05.002
- Winkelmann A, Trager-Cowan C, Sweeney F, Day AP, Parbrook P (2007) Many-beam dynamical simulation of electron backscatter diffraction patterns. *Ultramicroscopy* 107:414–421, DOI 10.1016/j.ultramic.2006.10.006
- Zuo J, Weickenmeier A (1995) On the beam selection and convergence in the Bloch-wave method. *Ultramicroscopy* 57(4):375–383, DOI 10.1016/0304 3991(94)00190-X

Electron Backscatter Diffraction in Materials Science

Schwartz, A.J.; Kumar, M.; Adams, B.L.; Field, D.P. (Eds.)

2009, XXII, 403 p., Hardcover

ISBN: 978-0-387-88135-5